frontiers | Frontiers in Earth Science

TYPE Original Research
PUBLISHED 11 October 2024
DOI 10.3389/feart.2024.1449515

OPEN ACCESS

EDITED BY
Bo Zhang,
Jilin University, China

REVIEWED BY
Xiaoyue Cao,
Key Laboratory of Exploration Technologies for Oil and Gas Resource (Yangtze University), China
Cong Zhou,
East China University of Technology, China
Rong Liu,
Central South University, China

*CORRESPONDENCE
Shijie Gao,
gsj@email.cugb.edu.cn

RECEIVED 15 June 2024
ACCEPTED 24 September 2024
PUBLISHED 11 October 2024

CITATION
Liu X and Gao S (2024) Response characteristics of 3D tensor CSAMT in axis anisotropic media.
Front. Earth Sci. 12:1449515.
doi: 10.3389/feart.2024.1449515

Response characteristics of 3D tensor CSAMT in axis anisotropic media

Xiao Liu[1] and Shijie Gao[2]*

[1]School of Hydraulic and Electric-power, Heilongjiang University, Harbin, China, [2]Institute of Geophysics, China Earthquake Administration, Beijing, China

Considering the significant impact of anisotropy on forward and inversion results, this paper presents a research study on tensor controlled-source audio magnetotellurics (CSAMT) forward modeling in axis anisotropic media. In this study, the tensor resistivity of axis anisotropic medium is introduced according to the control equation of electric field with sources. The total electric field is decomposed into primary and secondary fields, with the primary field obtained using Key's algorithm and the secondary field calculated using the finite difference method. This approach enables three-dimensional (3D) modeling of tensor CSAMT in axis anisotropic media. The correctness of the algorithm is verified by comparing it with the results obtained using a two-dimensional (2D) finite element algorithm. Several sets of axis anisotropic 3D models are designed, and the response characteristics of anisotropic target bodies to plane waves and non-plane waves are summarized. The findings indicate that the Cagniard resistivity and tipper are sensitive to changes in the X and Y directions of the anomaly, but not sensitive to changes in resistivity in the Z direction. Additionally, in the near region, non-plane wave CSAMT signals may cause distortion in the Cagniard resistivity. The results highlight that tensor CSAMT has the capability to detect changes in resistivity in two-axis directions (X and Y), providing greater exploration advantages compared to scalar CSAMT. This study provides a foundation for the forward modeling and inversion of tensor CSAMT in arbitrary anisotropic media.

KEYWORDS

tensor CSAMT, axis anisotropy, Cagniard resistivity, tipper, forward algorithm

1 Introduction

Controlled-source audio magnetotellurics has the advantages of high work efficiency and high signal-to-noise ratio. CSAMT has been widely used in fields such as geological exploration, oil, natural gas, geothermal, metal mineral exploration, and hydrological and environmental engineering fields (Xue et al., 2015; Guo et al., 2019; Xu et al., 2020; Di et al., 2020).

Scalar CSAMT can be divided into equatorial and axial devices. Both use a field source to excite and collect two components (E_x, H_y or E_y, H_x) in the receiving region. Tensor CSAMT uses two directional field sources to measure five components

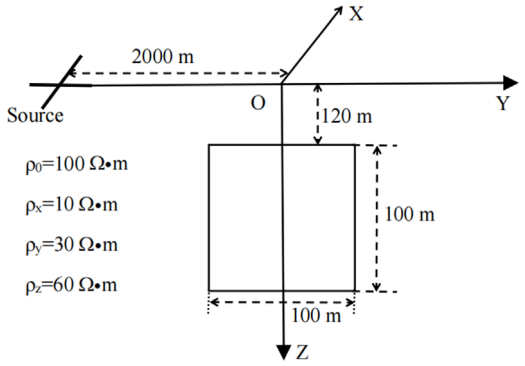

FIGURE 1
Sketch of 2D model.

(E_x, E_y, H_x, H_y, and H_z). In complex geological conditions, tensor CSAMT can fully describe 3D geoelectric information (Caldwell et al., 2002), effectively improving exploration accuracy, with more advantages than scalar CSAMT. Li and Pedersen (1991), Boerner et al. (1993), and Garcia et al. (2003) pioneered the development of tensor CSAMT. The research on tensor CSAMT forward modeling and inversion in isotropic media is becoming increasingly mature (Wang G. et al., 2018; Chen et al., 2020; Hui, 2021; Cao et al., 2021).

Among the factors that directly affect the results of forward modeling and inversion, anisotropy has a significant impact. Considering that anisotropy is very common in areas with well-developed stratigraphic layers, it is necessary to develop electromagnetic data processing and inversion methods in anisotropic media to improve the accuracy of inversion and the level of geological interpretation (Liu et al., 2018). The use of electrical anisotropy information can deepen our understanding of the structure of the Earth's lithosphere, the laws of material transport in deep Earth, and the dynamic processes in deep Earth (Kirkby et al., 2015).

Yin et al. (2014) performed a 3D forward modeling study of marine controlled-source electromagnetic method using a staggered finite difference technique to analyze the influence of seabed conductivity anisotropy on shallow sea data. Cai et al. (2015) used the scalar finite element method to obtain the response of CSAMT with anisotropic conductivity. Li et al. (2017) and He et al. (2019) applied the vector finite element method to achieve anisotropic forward modeling of CSAMT. These studies showed the significant impact of axis anisotropic tensor conductivity on the response results of CSAMT, especially the amplitude and distribution characteristics of apparent resistivity (Qiu et al., 2018).

There have been relatively few studies on tensor CSAMT forward modeling and inversion on axis anisotropic media (Wang K. P. et al., 2018; Liu and Zheng, 2024). No research results on tensor CSAMT forward modeling and inversion of arbitrary anisotropy have been published. Wang and Tan et al. (2017) and Wang et al. (2017) demonstrated through finite difference forward modeling that tensor CSAMT can identify at least two horizontal resistivities through multi-component observations, and provides some help for the preliminary qualitative interpretation of tensor CSAMT. Their research focused on how to achieve axis anisotropic inversion.

Based on the study of isotropic media, this study applies the finite difference method (Xie et al., 2016) to tensor CSAMT research on axis anisotropy, analyzes the influence of axis anisotropy on the forward modeling results of tensor CSAMT, and summarizes the response characteristics of anisotropic target bodies with plane waves and non-plane waves. The study provide a foundation for the forward modeling and inversion of tensor CSAMT in arbitrary anisotropic media.

2 Forword modeling method

2.1 Finite difference method for calculating electromagnetic fields

For isotropic media, ignoring displacement current, under the excitation condition of an electrical source, the electric field **E** satisfies the following equation (Li and Key, 2007):

$$\nabla \times \nabla \times \mathbf{E} = i\omega\mu_0(\sigma\mathbf{E} + \mathbf{J}_s) \tag{1}$$

where ∇ represents the Nabla operator, i represents an imaginary unit, ω represents the angular frequency, μ_0 represents the vacuum magnetic permeability, σ represents the conductivity, and $\mathbf{J}_s$ represents the current density excited by an external electrical source.

The total field **E** is composed of primary $\mathbf{E}^p$ and secondary fields $\mathbf{E}^s$. Equation 1 is transformed to obtain the following electric field control equation:

$$\nabla \times \nabla \times \mathbf{E}^s - i\omega\mu_0\sigma\mathbf{E}^s = i\omega\mu_0(\sigma - \sigma_0)\mathbf{E}^p \tag{2}$$

In axis anisotropic media, the tensor conductivity is

$$\boldsymbol{\sigma} = \begin{pmatrix} \sigma_{xx} & 0 & 0 \\ 0 & \sigma_{yy} & 0 \\ 0 & 0 & \sigma_{zz} \end{pmatrix} \tag{3}$$

Substitute Equation 3 into Equation 2 and organize it to obtain the following equation for the three components of the electric field:

$$\frac{\partial}{\partial y}\left[\frac{\partial E_y^s}{\partial x} - \frac{\partial E_x^s}{\partial y}\right] - \frac{\partial}{\partial z}\left[\frac{\partial E_x^s}{\partial z} - \frac{\partial E_z^s}{\partial x}\right] - i\omega\mu_0\sigma_{xx}E_x^s = i\omega\mu_0(\sigma_{xx} - \sigma_p)E_x^p \tag{4}$$

$$\frac{\partial}{\partial z}\left[\frac{\partial E_z^s}{\partial y} - \frac{\partial E_y^s}{\partial z}\right] - \frac{\partial}{\partial x}\left[\frac{\partial E_y^s}{\partial x} - \frac{\partial E_x^s}{\partial y}\right] - i\omega\mu_0\sigma_{yy}E_y^s = i\omega\mu_0(\sigma_{yy} - \sigma_p)E_y^p \tag{5}$$

$$\frac{\partial}{\partial x}\left[\frac{\partial E_x^s}{\partial z} - \frac{\partial E_y^s}{\partial x}\right] - \frac{\partial}{\partial y}\left[\frac{\partial E_z^s}{\partial y} - \frac{\partial E_y^s}{\partial z}\right] - i\omega\mu_0\sigma_{zz}E_z^s = i\omega\mu_0(\sigma_{zz} - \sigma_p)E_z^p \tag{6}$$

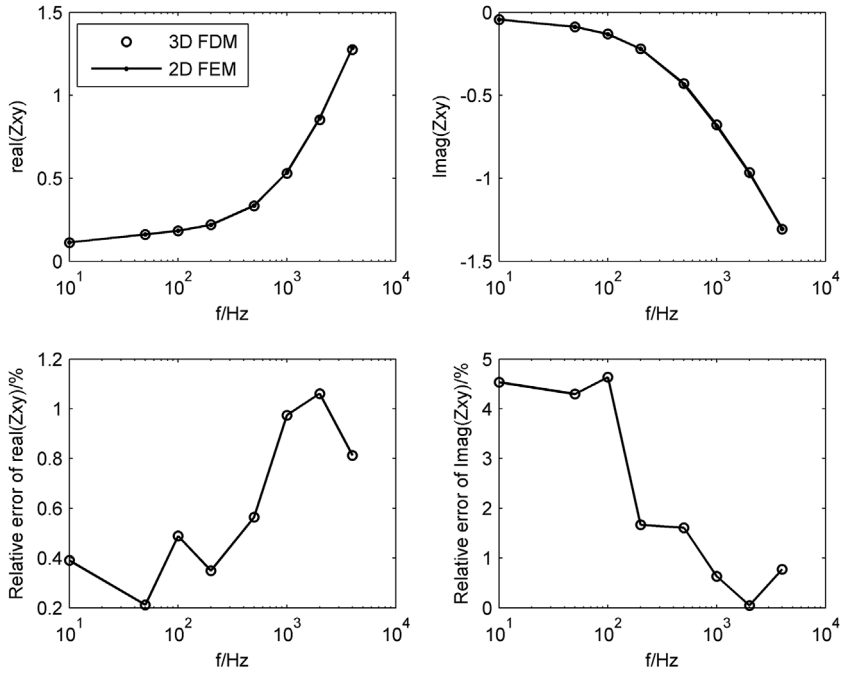

FIGURE 2
Comparison of the results of 3D FDM and 2D FEM results.

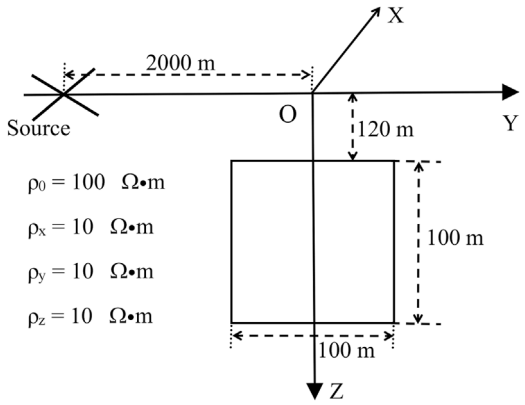

FIGURE 3
Sketch of the 3D model.

The calculation method for the electric field $\mathbf{E}^p$ is in a 1D medium which is the same as Key's method (Key, 2009). In the Cartesian coordinate system, the 3D staggered sampling Yee's grid is applied to discretize Equations 4–6. Define the electric field at the center of each grid cell edge and the magnetic field at the center of each grid cell surface. Use forward difference approximation differentiation to obtain a large linear equation system of the quadratic electric field at each network cell node in the entire partition area. As follows,

$$\mathbf{K}\mathbf{E}^s = \mathbf{s} \tag{7}$$

where $\mathbf{K}$ is a symmetric large sparse coefficient matrix, $\mathbf{E}^s$ is a column vector composed of the three components of the secondary electric field to be solved, $\mathbf{s}$ is the right column vector, and is related to the values of the primary field and boundary field.

Set the secondary field values at the top boundary, four side boundaries, and underground bottom boundary of the study area to zero as the boundary condition. The quasi minimum residual (QMR) method is used to solve Equation 7, and divergence correction is introduced during the iteration process (Siripunvaraporna et al., 2002; Liu and Sun, 2024), to obtain the three component values of the electric field in the entire space. Interpolation method is used to calculate the electromagnetic field components values of measurement points on the surface.

2.2 Calculating tensor impedance and tipper

Tensor CSAMT is excited by two field sources with different polarization directions. This study uses a "+" shaped orthogonal field source to excite in two directions, that is, the forward calculation for each frequency requires solving Equation 7 twice. Collect five electromagnetic field components in the receiving area, denoted as E_{x1}, E_{y1}, H_{x1}, H_{y1} and H_{z1}, E_{x2}, E_{y2}, H_{x2}, H_{y2} and H_{z2}.

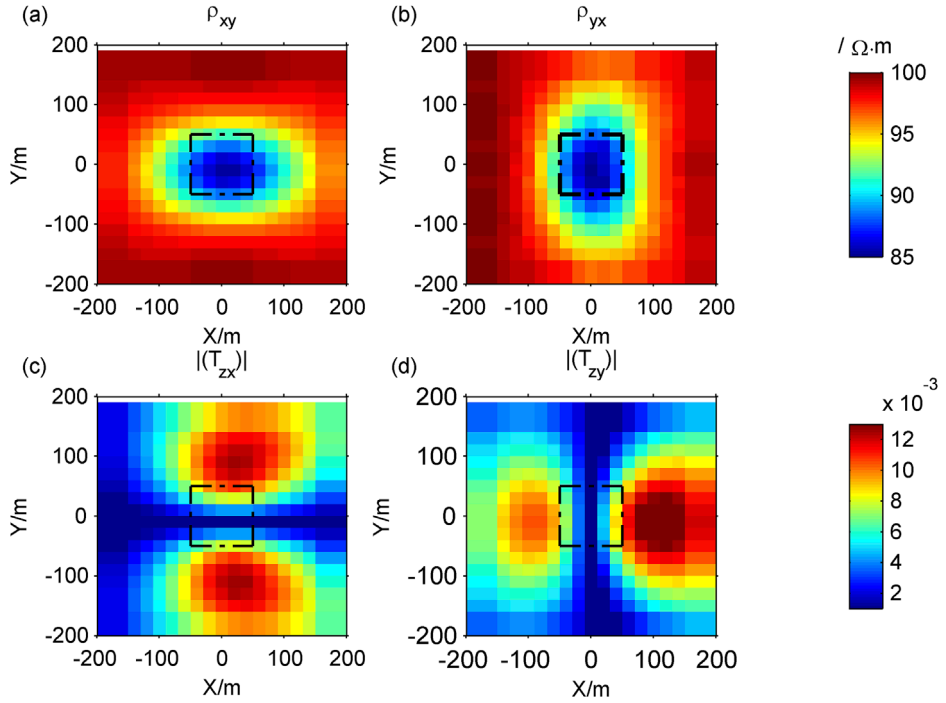

FIGURE 4
Response of the 3D model. **(A)** ρ_{xy}, **(B)** ρ_{yx}, **(C)** $|T_{zx}|$, and **(D)** $|T_{zy}|$.

TABLE 1 The axis anisotropic model.

Axis anisotropic model	X	Y	Z
resistivity/ $\Omega \cdot m$	10 30 60 1,000	30 30 30 30	60 60 60 60
	10 10 10	10 60 1,000	60 60 60
	10 10 10	30 30 30	10 30 1,000

The expressions for the main diagonal impedance components and tipper are as follows:

$$Z_{xy} = \frac{E_{x2}H_{y1} - E_{x1}H_{x2}}{H_{x1}H_{y2} - H_{x2}H_{y1}},\ Z_{yx} = \frac{E_{y1}H_{y2} - E_{y2}H_{y1}}{H_{x1}H_{y2} - H_{x2}H_{y1}} \tag{8}$$

$$T_{zx} = \frac{H_{z1}H_{y2} - H_{z2}H_{y1}}{H_{x1}H_{y2} - H_{x2}H_{y1}},\ T_{zy} = \frac{H_{z2}H_{x1} - H_{z1}H_{x2}}{H_{x1}H_{y2} - H_{x2}H_{y1}} \tag{9}$$

The corresponding Cagniard resistivity equation is:

$$\rho_{ij} = \frac{1}{\omega\mu_0}\left|Z_{ij}\right|^2 \tag{10}$$

where $i = x, y$, $j = x, y$. In the following text, the axis anisotropy response of CSAMT is calculated by Equations 8–10.

2.3 Algorithm validation

The algorithm is written in Fortran language. To verify the correctness of the algorithm, we designed a 2D model and compared it with the finite element method results of Key (2016). The background resistivity is 100 $\Omega \cdot m$, the direction of the anomalous body is parallel to the X-axis direction, buried at a depth of 120 m. The prism has a size of 100 m × 100 m. The resistivity in the X, Y, and Z directions is 10, 30, and 60 $\Omega \cdot m$, respectively (Figure 1). The lengths of the two intersecting ground wire sources are 100 m, parallel to the Y-axis and X-axis, with a current of 10 A. The transmission frequencies are 10, 50, 100, 200, 500, 1,000, 2,000, and 4,000 Hz, and the receiving point is located at the origin. The line source parallel to the X-axis (Figure 1) corresponds to an equatorial device and can measure E_{x1}, H_{y1}. Similarly, a line source parallel to the Y-axis (Figure 1) corresponds to an axial device and can measure E_{y2}, H_{y2}. These components are then utilized in the calculation of Z_{xy} and Z_{yx}.

The comparison of impedance results between the two methods is shown in Figure 2. The real and imaginary parts of Z_{xy} calculated by the finite difference method and Key's finite element method match very well (Figure 2). The maximum relative error is less than 5%, indicating that the calculation results of the tensor CSAMT 3D forward algorithm are correct (Liu et al., 2021).

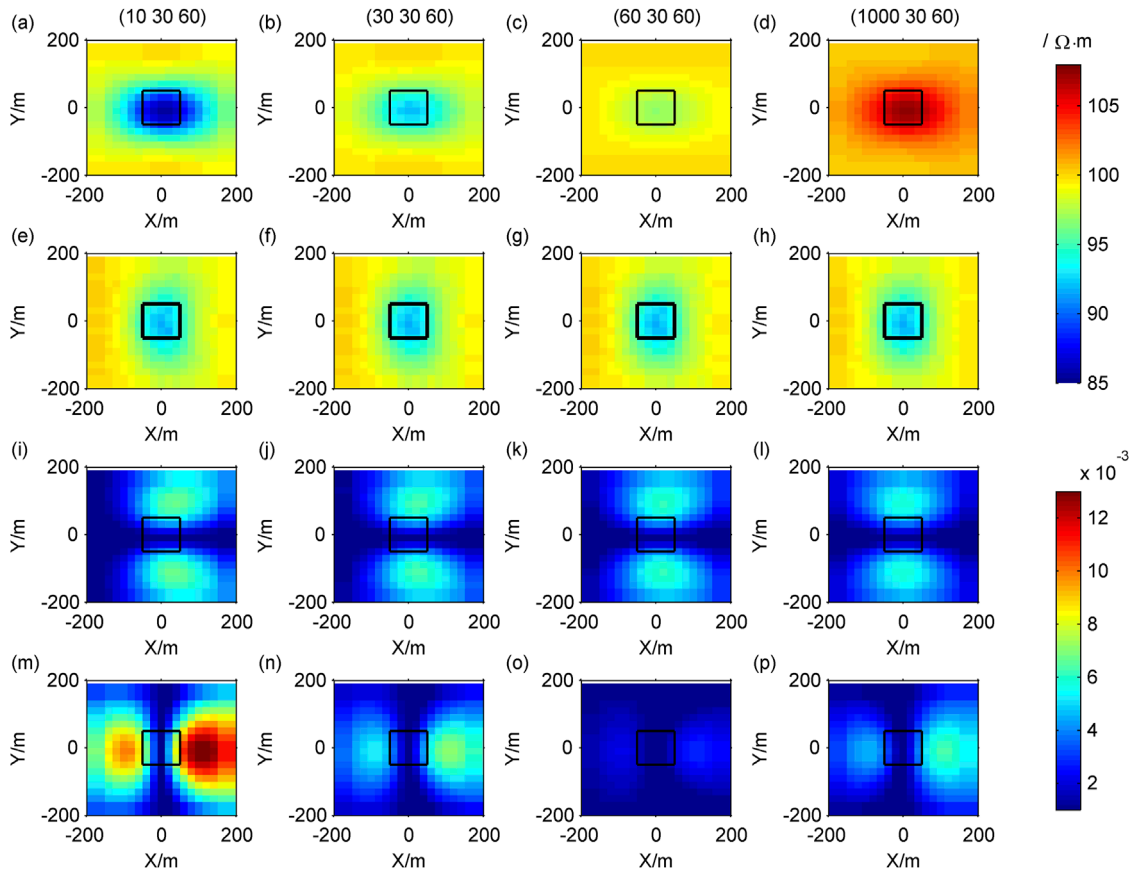

FIGURE 5
Contour maps of response of different resistivity in the X direction: **(A–D)** ρ_{xy}; **(E–H)** ρ_{yx}; **(I–L)** $|T_{zx}|$; **(M–P)** $|T_{zy}|$.

3 Forward modeling case

3.1 Response characteristics of low-resistance model

The 3D low-resistance prism model is shown in Figure 3, with a background resistivity of 100 $\Omega \cdot m$ and a buried depth of 120 m. The prism has a size of 100 m × 100 m × 100 m, and the resistivity in the X, Y, and Z directions is 10 $\Omega \cdot m$. The prism is projected at the center of the surface as the origin.

The centers of two intersecting ground wire sources are located at −2,000 m on the Y-axis, with a length of 100 m and angle of 45° and 135° with the Y-axis, respectively. The transmission frequency is 500 Hz. The finite difference mesh is 33 × 42 × 41 (including 12 air layers).

The forward results of the low-resistance model are shown in Figure 4. It is evident that the Cagniard resistivity ρ_{xy} and ρ_{yx} contours exhibits a notable low-value anomaly, aligning with the horizontal position of the low-resistance body (Figures 4A, B). T_{zx} and T_{zy} reflect the horizontal boundary of the low-resistance body (Figures 4C, D).

3.2 Influence of anisotropy on response characteristics

The study by Wang et al. (2017) demonstrated that when the resistivity of the axis anisotropic model in the X direction is the same as that of the isotropic model, the apparent resistivity of the XY-mode is almost the same. When the resistivity of the axis anisotropic model in the Y direction is the same as that of the isotropic model, the apparent resistivity of the YX-mode in both models are almost the same. To illustrate the impact of changes in the axis anisotropy of low-resistance bodies on the forward response, we established three sets of axis anisotropy resistivity models (Table 1) to simulate the resistivity changes of anomalous bodies in the X, Y, and Z directions.

The size of the low-resistance model and the parameters of the source are the same as the example in section 3.1.

The transmission frequency of the source is 500 Hz. At this time, the CSAMT signal is approximately a plane wave. We first fix the resistivity of the low-resistance body in the Y and Z directions to 30 and 60 $\Omega \cdot m$, respectively, with the resistivity in the X direction of 10, 30, 60, and 1,000 $\Omega \cdot m$, respectively, the forward results are shown in Figure 5. Next, we fix the resistivity of the low-resistance body

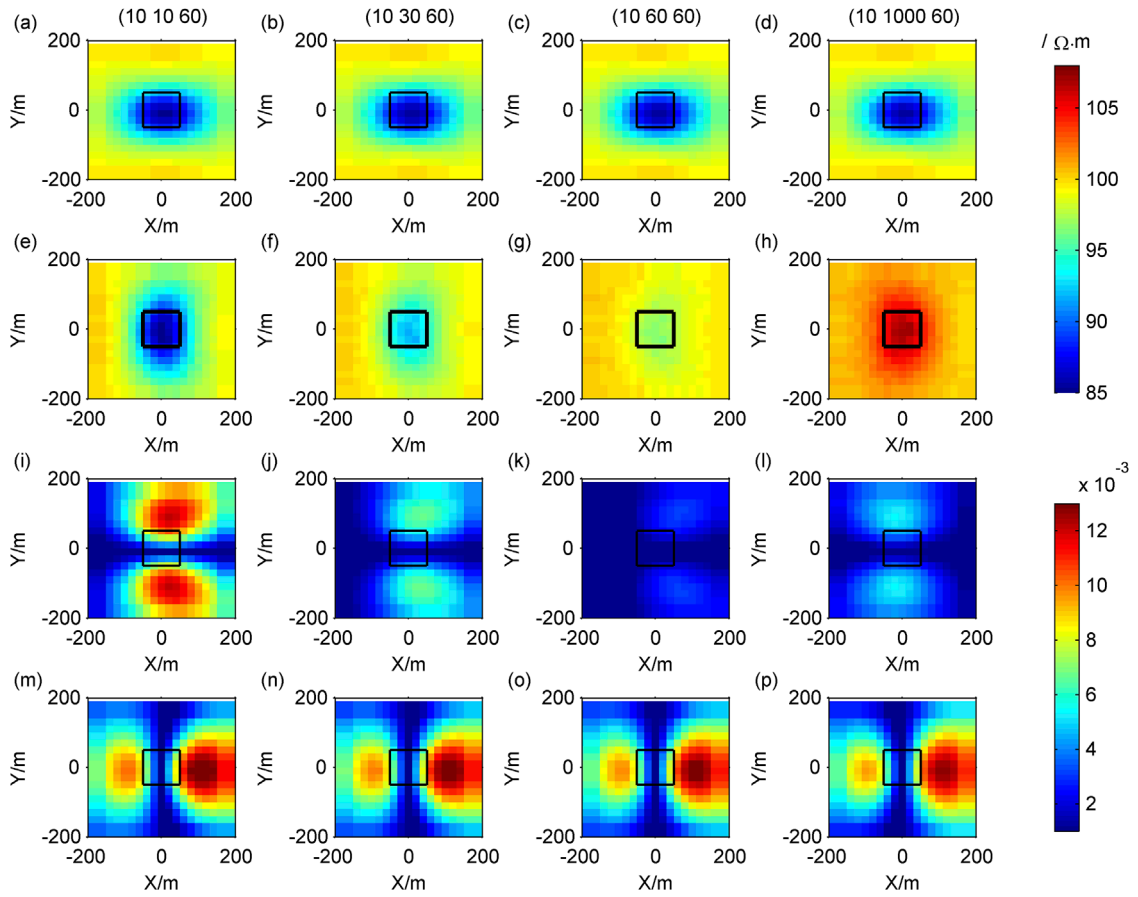

FIGURE 6
Contour maps of response of different resistivity in the Y direction: **(A–D)** ρ_{xy}; **(E–H)** ρ_{yx}; **(I–L)** $|T_{zx}|$; **(M–P)** $|T_{zy}|$.

in the X and Z directions to 10 and 60 $\Omega \cdot m$, respectively, with the resistivity in the Y direction of 10, 60, and 1,000 $\Omega \cdot m$, respectively, the forward results are shown in Figure 6. Finally, we fix the resistivity of the low-resistance body in the X and Y directions to 10 and 30 $\Omega \cdot m$, respectively, with the resistivity in the Z direction of 10, 30, 60, and 1,000 $\Omega \cdot m$, respectively, the forward results are shown in Figure 7.

The Cagniard resistivity ρ_{xy} is highly sensitive to changes in resistivity in the X direction of the anomalous body. Its amplitude is determined by the resistivity in the X direction and exhibits a low-value anomaly for low-resistance bodies, which diminishes as the resistivity of the low-resistance body increases (Figures 5A–D). Conversely, high-resistance bodies display high-value anomalies with small amplitudes. ρ_{yx} and $|T_{zx}|$, however, are not sensitive to changes in resistivity in the X direction of the anomalous body (Figures 5E–L). The $|T_{zy}|$ decreases as the resistivity of the low-resistance body increases (Figures 5M–P).

Similarly, ρ_{xy} and $|T_{zy}|$ are not sensitive to changes in resistivity in the Y direction of the anomalous body (Figures 6A–D; Figures 6M–P). On the other hand, ρ_{yx} is very sensitive to changes in resistivity in the Y direction. Its amplitude is determined by the resistivity in the Y direction and exhibits low-value anomalies for low-resistance bodies (Figures 6E–H). The amplitude of these anomalies decreases as the resistivity of the low-resistance body increases. For high-resistance bodies, ρ_{yx} exhibits high-value anomalies with small amplitudes. $|T_{zx}|$ also decreases as the resistivity of the low-resistance body increases (Figures 6I–L). Both the Cagniard resistivity and the modulus of tipper are not sensitive to changes in resistivity in the Z direction (Figures 7A–P).

In CSAMT, in the XY-mode, the polarization direction of the electric field is mainly in the X direction, making it sensitive to the electrical resistivity of the low-resistance body in the X direction. In the YX-mode, the polarization direction of the electric field is primarily in the Y direction, making it sensitive to the resistivity of low-resistance bodies in the Y direction.

3.3 Impact of model size on response characteristics

To illustrate the impact of changes in model size on forward response, we set up three sets of axis anisotropic

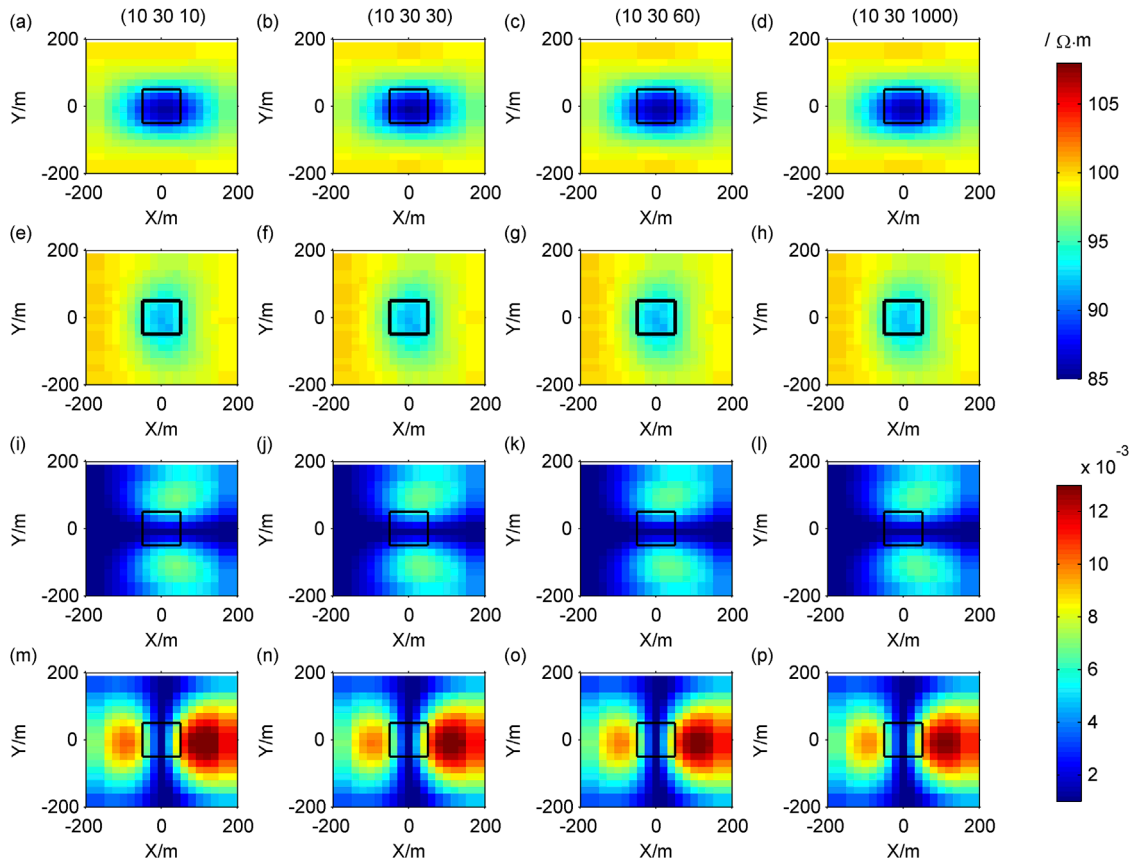

FIGURE 7
Contour maps of response of different resistivity in the Z direction: **(A–D)** ρ_{xy}; **(E–H)** ρ_{yx}; **(I–L)** $|T_{zx}|$; **(M–P)** $|T_{zy}|$.

TABLE 2 Axis anisotropic low-resistance model.

Model	length/m	width/m	height/m
axis anisotropic model	40 100 180	100 100 100	100 100 100
	100 100 100	40 100 180	100 100 100
	100 100 100	100 100 100	40 100 180

resistivity models (Table 2), to represent the length, width, and height changes of anomalous bodies in the X, Y, and Z directions, respectively. The resistivity in the X, Y, and Z directions are 10, 30, and 60 $\Omega \cdot m$, respectively, and the source parameters are the same as the example in the section 3.1.

We first fix the width and height of the low-resistance body to 100 m, with the length in the X direction of 40, 100, and 180 m, respectively, the forward results are shown in Figure 8. Next, we fix the length and height of the low-resistance body to 100 m, with the width in the Y direction of 40, 100, and 180 m, respectively, the forward results are shown in Figure 9. Finally, we fix the length and width of the low-resistance body to 100 m, with the height in the Z direction of 40, 100, and 180 m, respectively, the forward results are shown in Figure 10.

As the length, width and height of the anomalous body increase, both the modulus of Cagniard resistivity anomaly and the modulus of tipper increase, leading to an expansion of the anomalous area (Figures 8–10).

The boundary of the ρ_{xy} anomaly area appears sharp in the Y direction and fuzzy in the X direction (Figures 8A–C; Figures 9A–C), indicating that it provides a better representation of the horizontal position of the anomalous body in the Y direction compared to the X direction. Conversely, the boundary of the ρ_{yx} anomaly area appears sharp in the X direction and fuzzy in the Y direction (Figures 8D–F; Figures 9D–F), indicating that it better reflects the horizontal position of the anomalous body in the X direction than in the Y direction. $|T_{zx}|$ can reflect the horizontal boundary of the anomalous body in the Y direction, while $|T_{zy}|$ can reflect the horizontal boundary in the X direction (Figures 8G–I; Figures 9G–I).

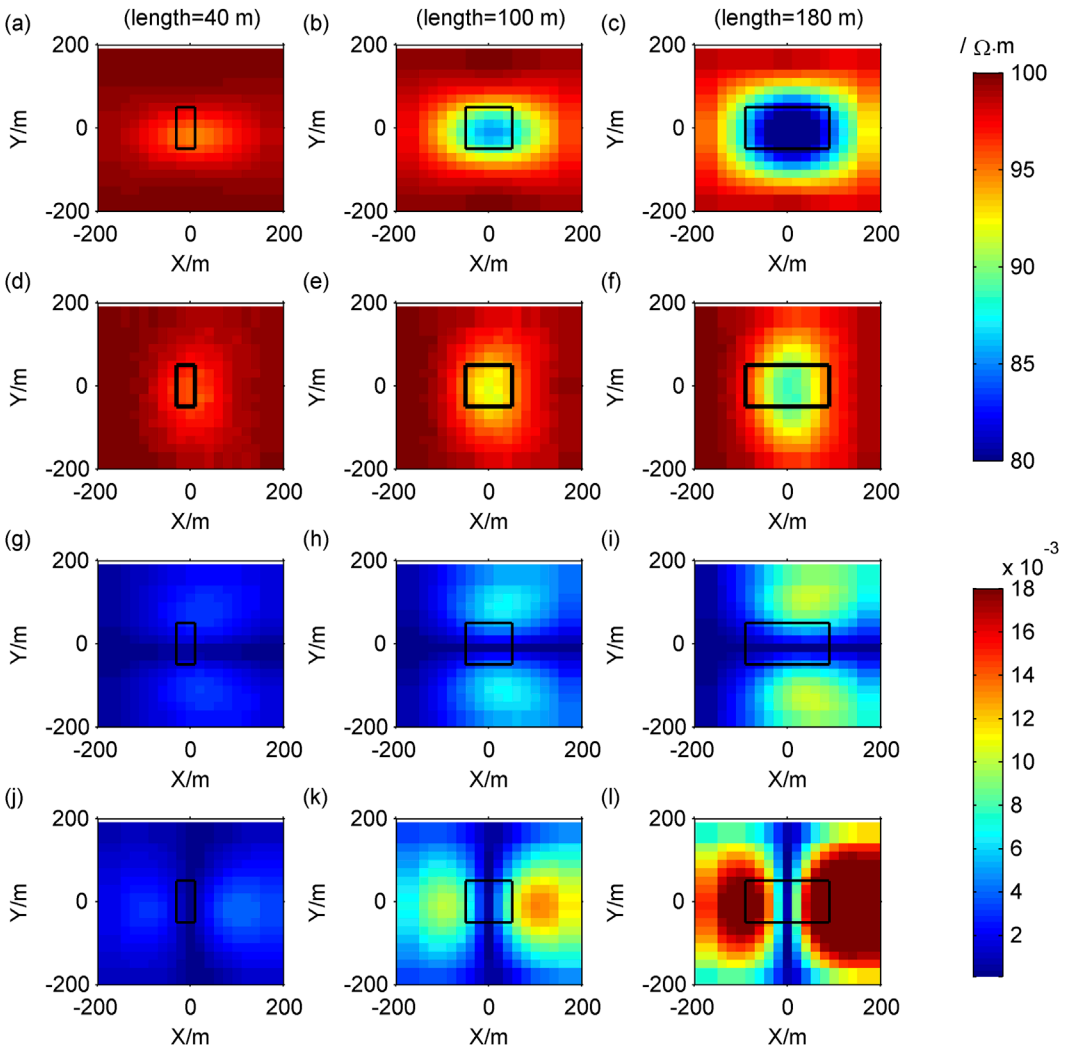

FIGURE 8
Contour maps of response when the length of model changes: **(A–C)** ρ_{xy}; **(D–F)** ρ_{yx}; **(G–I)** $|T_{zx}|$; **(J–L)** $|T_{zy}|$.

3.4 Response of axis anisotropic complex prism model

Here, a prism model is established with a top burial depth of 120 m. The plan of the model is shown in Figure 11, and the resistivity in the X, Y, and Z directions is 10, 1,000, and 100 $\Omega \cdot m$, respectively. The parameters of the source are the same as the examples in the previous section, and the model response is shown in Figure 12.

The low-value anomaly area in the contour map of ρ_{xy} corresponds to the low resistance area in the X direction of the anomaly body (Figure 12A), while the high-value anomaly area in the contour map of ρ_{yx} corresponds to the high resistance area in the Y direction of the anomaly body (Figure 12B). The tippers reflect the horizontal boundary of the anomaly body (Figures 12C, D), which is the same as the characteristics in the previous example.

3.5 Response in non-plane wave areas

For case 3.2, when the transmission frequency of the source is 10 Hz, the receiving region belongs to the near-field areas, and the CSAMT signal is a non-plane wave. When the resistivity in the X direction changes, the forward modeling results are shown in Figure 13, and the curve of the Cagniard resistivity with frequency at the center point of the receiving region is shown in Figure 14. When the resistivity in the Y direction changes, the forward modeling results are shown in Figure 15, and the curve of the Cagniard resistivity with frequency at the center point of the receiving region is shown in Figure 16.

Compared with the response of plane waves (Figures 5A–D), the Cagniard resistivity ρ_{xy} of non-plane waves is distorted with a high-value anomaly (Figures 13A–D), which increases as the resistivity in the X direction of the anomalous body increases (Figure 14A). The Cagniard resistivity ρ_{yx} of non-plane wave

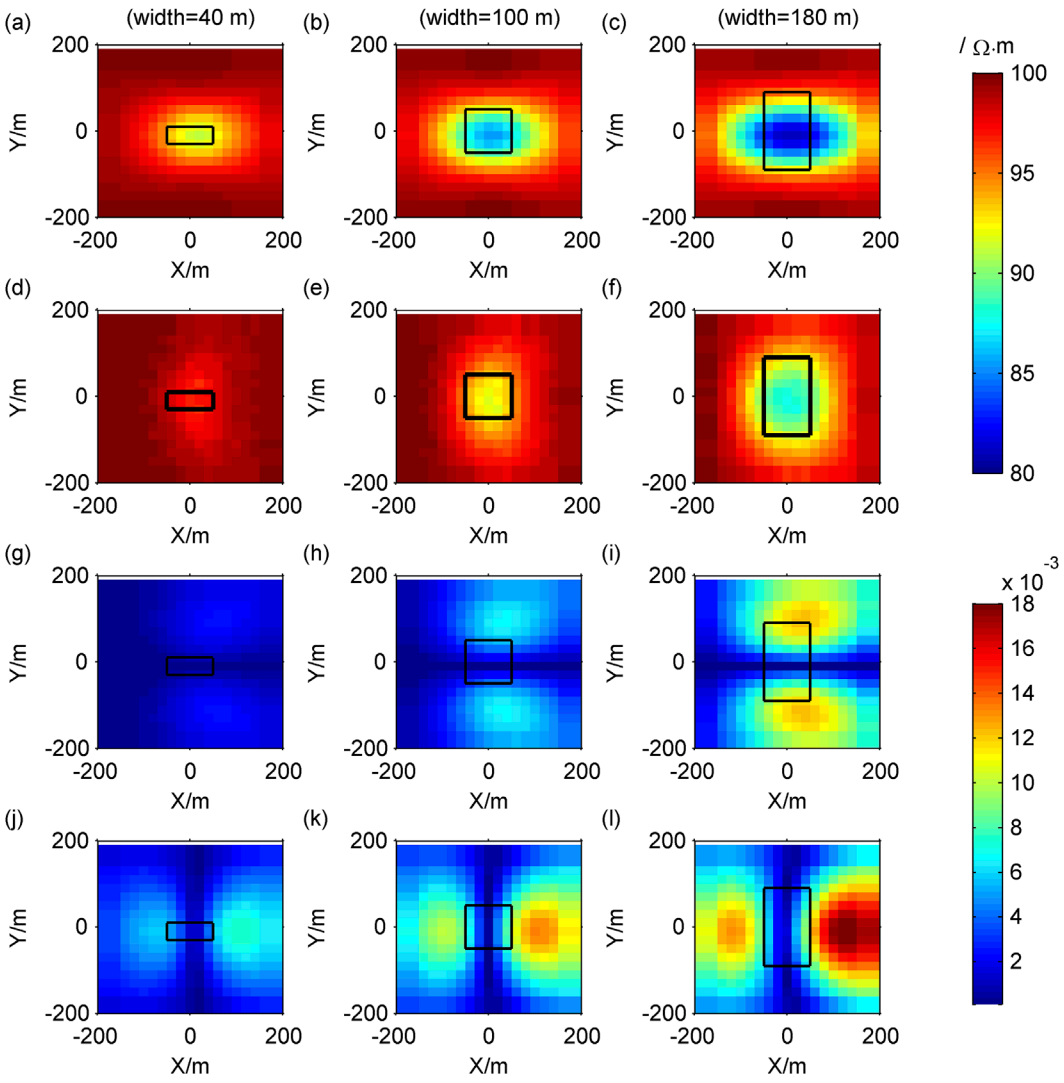

FIGURE 9
Contour maps of response when the width of the model changes: **(A–C)** ρ_{xy}; **(D–F)** ρ_{yx}; **(G–I)** $|T_{zx}|$; **(J–L)** $|T_{zy}|$.

signals is distorted and insensitive to the changes in resistivity in the X direction of the anomalous body (Figures 13E–H; Figure 14B). The characteristics of the tippers of non-plane waves (Figures 13I–P) are similar to those of plane waves (Figures 5I–P).

The ρ_{xy} of non-plane wave signals is distorted and insensitive to the changes in resistivity in the Y direction of the anomalous body (Figures 5A–D; Figure 16A). Compared with the response of plane waves (Figures 6E–H), the ρ_{yx} of non-plane waves is distorted and sensitive to the changes in resistivity in the Y direction of the anomalous body (Figures 15E–H). ρ_{yx} increases as the resistivity in the Y direction of the anomalous body increases (Figure 16B). The characteristics of the tippers of non-plane waves (Figures 15I–P) are similar to those of plane waves (Figures 6I–P).

Whether it is an isotropic medium or an anisotropic medium, the CSAMT apparent resistivity in the near region will be distorted and needs to be corrected.

4 Conclusion

This study utilizes the 3D finite difference method to perform tensor CSAMT forward modeling in axis anisotropic media. The correctness of the algorithm is validated by comparing the results with Key's 2D finite element algorithm. The forward modeling examples demonstrate that Cagniard resistivity exhibits low-value anomalies for low-resistance bodies and high-value anomalies for high-resistance bodies. Tippers are capable of reflecting the horizontal boundaries of anomalous bodies. The

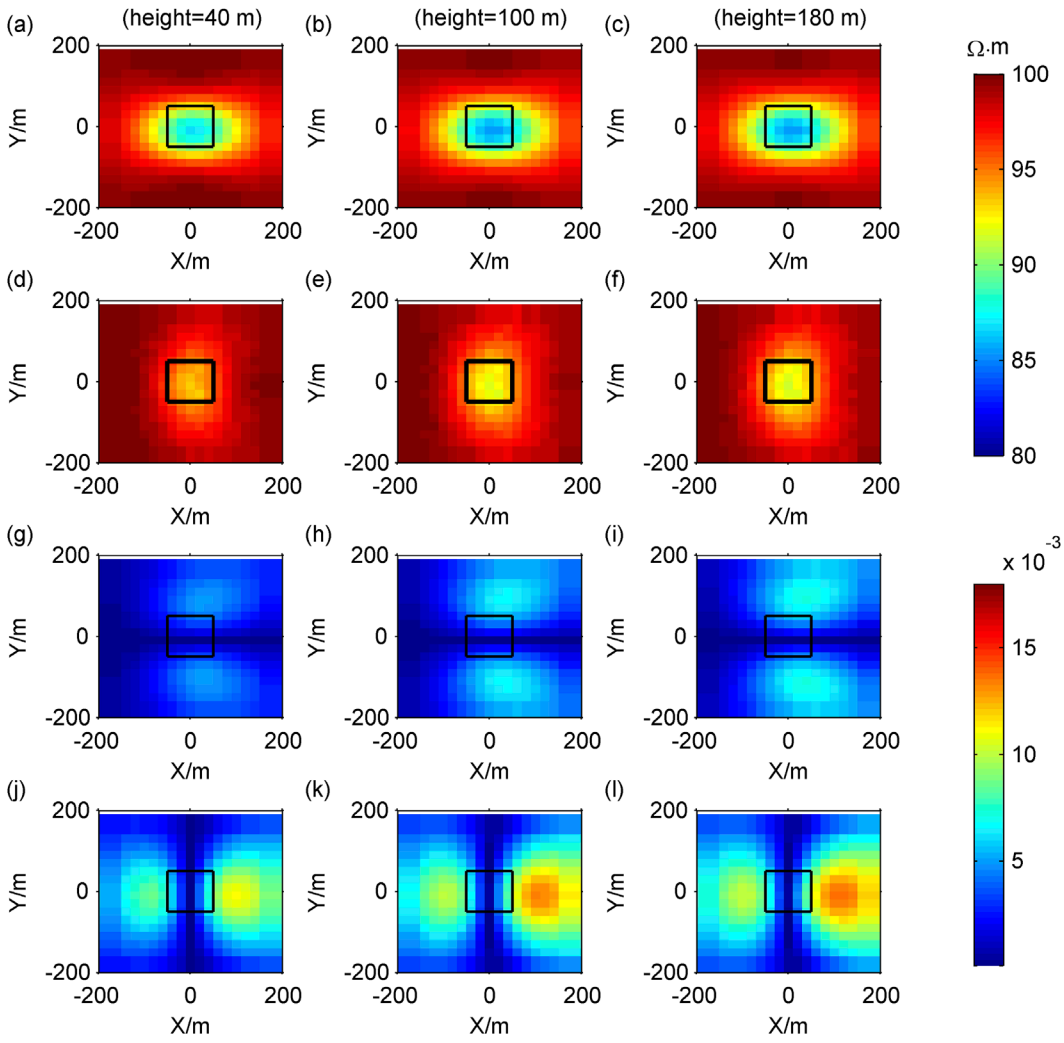

FIGURE 10
Contour maps of response when the width of the model changes: **(A–C)** ρ_{xy}; **(D–F)** ρ_{yx}; **(G–I)** $|T_{zx}|$; **(J–L)** $|T_{zy}|$.

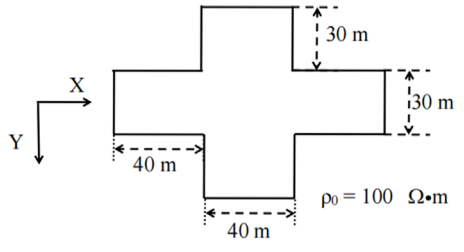

FIGURE 11
Sketch of 3D axis anisotropic prism model.

resistivity changes of the anomalous body are found to have different sensitivities in the X and Y directions, influenced by the polarization direction of the electric field. Specifically, ρ_{xy} and $|T_{zy}|$ are sensitive to changes in resistivity in the X direction, while ρ_{yx} and $|T_{zx}|$ are sensitive to changes in the resistivity in the Y direction. However, the Cagniard resistivity and tipper exhibit poor sensitivity to changes in the resistivity of the anomalous body in the Z direction. The amplitude of ρ_{xy} is determined by the resistivity in the X direction of the anomalous body and displays the horizontal position of the anomalous body in the Y direction better than in the X direction. Similarly, the amplitude of ρ_{yx} is determined by the resistivity in the Y direction and performs better in displaying the horizontal position of anomalous bodies in the Y direction than in the X direction.

In the near region, the CSAMT signal of non-plane waves induces distortion in the Cagniard resistivity. The characteristics of tippers for non-plane waves are similar to those of plane waves. When exploring anisotropic media, tensor CSAMT proves advantageous in identifying changes in resistivity in two-axis (X and Y) directions compared to scalar CSAMT.

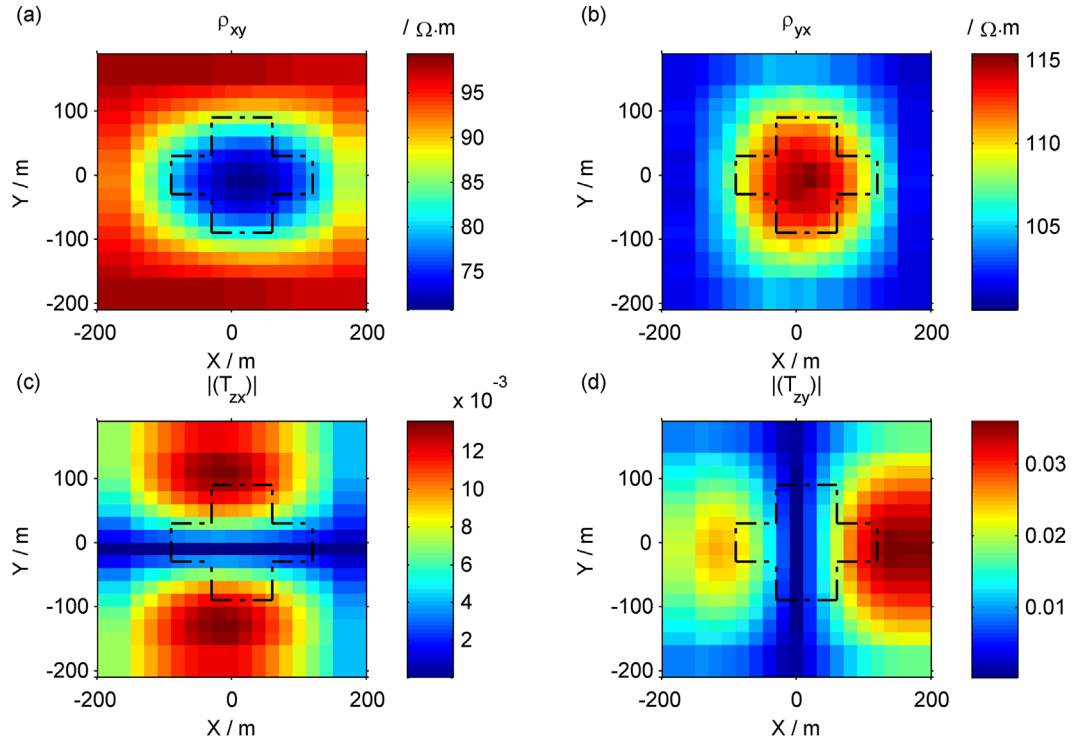

FIGURE 12
Response of the 3D anisotropic prism model. **(A)** ρ_{xy}, **(B)** ρ_{yx}, **(C)** $|T_{zx}|$, and **(D)** $|T_{zy}|$.

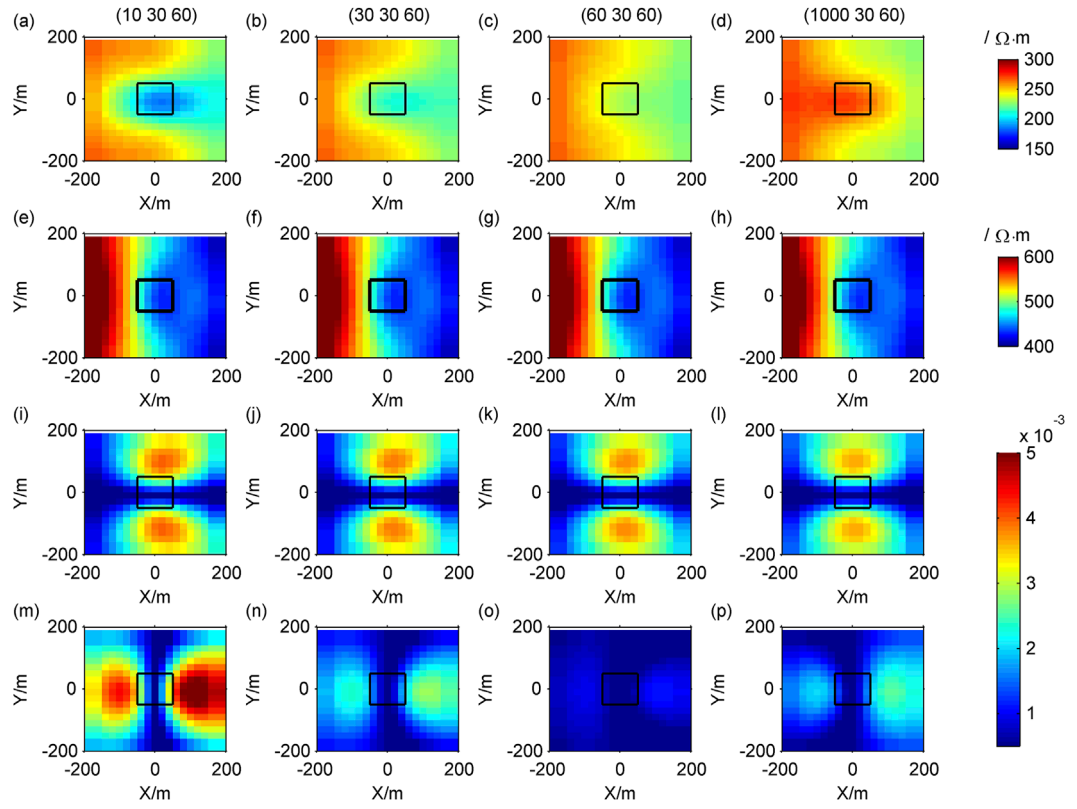

FIGURE 13
For non-plane waves, the contour maps of response of different resistivity in the X direction: **(A–D)** ρ_{xy}; **(E–H)** ρ_{yx}; **(I–L)** $|T_{zx}|$; **(M–P)** $|T_{zy}|$.

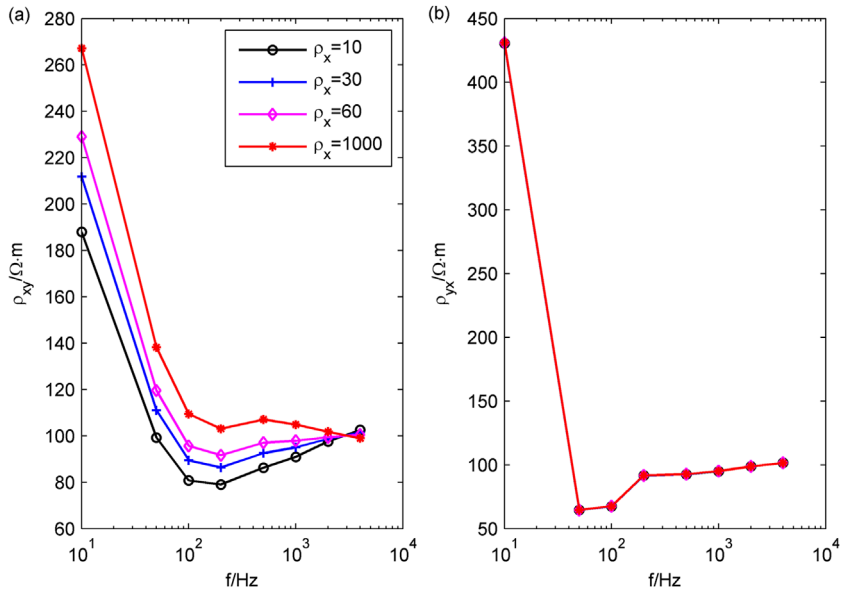

FIGURE 14
The curve of Cagniard resistivity with frequency at the center point of the receiving region when the resistivity changes in the X direction. **(A)** ρ_{xy}, **(B)** ρ_{yx}.

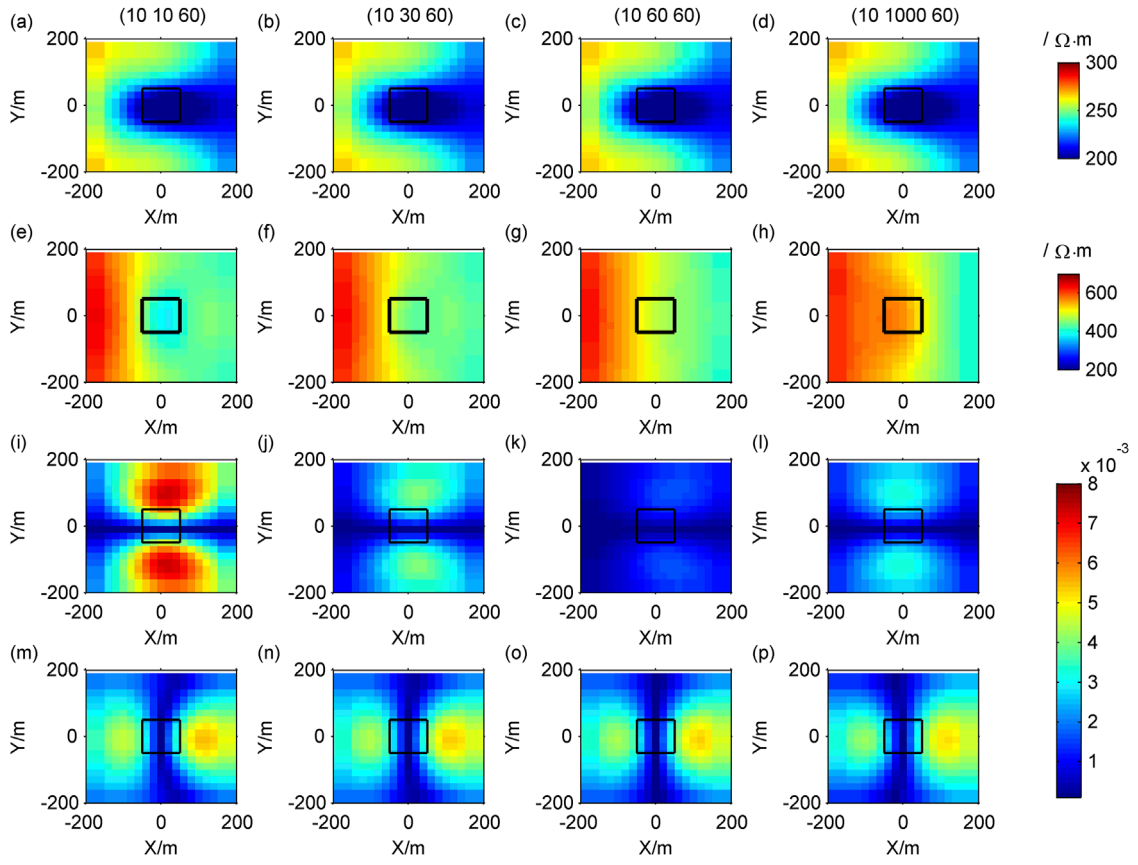

FIGURE 15
For non-plane waves, the contour maps of response of different resistivity in the Y direction: **(A–D)** ρ_{xy}; **(E–H)** ρ_{yx}; **(I–L)** $|T_{zx}|$; **(M–P)** $|T_{zy}|$.

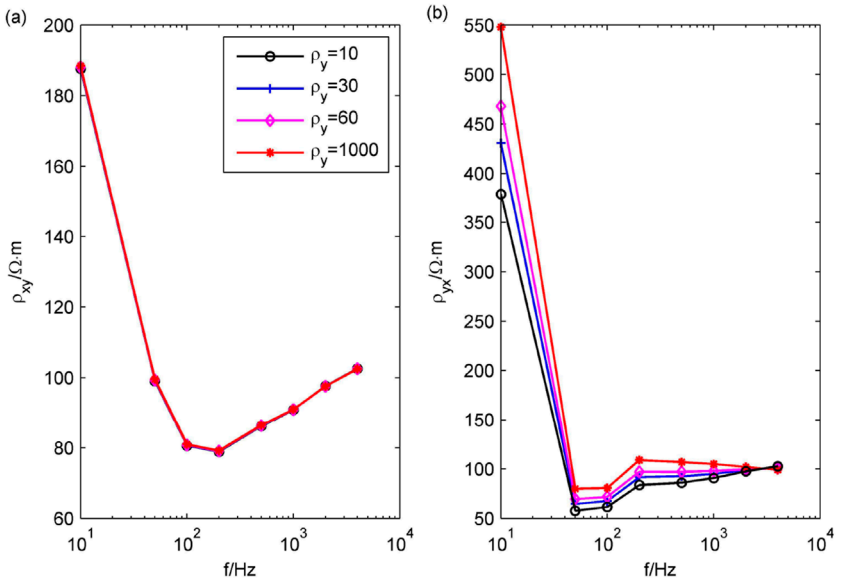

FIGURE 16
The curve of Cagniard resistivity with frequency at the center point of the receiving region when the resistivity changes in the Y direction. **(A)** ρ_{xy}, **(B)** ρ_{yx}.

Whether utilizing the MT method (Kong et al., 2023) or the CSAMT method, the Cagniard resistivity and tipper demonstrate poor sensitivity to resistivity changes in the Z direction. Therefore, investigating methods to improve the identification of anisotropic Z direction (vertical) resistivity using electromagnetic techniques is a topic worthy of further study.

Data availability statement

The raw data supporting the conclusions of this article will be made available by the authors, without undue reservation.

Author contributions

XL: Conceptualization, Data curation, Formal Analysis, Funding acquisition, Investigation, Methodology, Project administration, Resources, Software, Validation, Visualization, Writing–original draft, Writing–review and editing. SG: Conceptualization, Supervision, Validation, Writing–review and editing.

Funding

The author(s) declare that financial support was received for the research, authorship, and/or publication of this article. This work is funded financially by Heilongjiang Province Basic Research Business Expenses for Universities Heilongjiang University Special Fund Project (Grant No. 2023-KYYWF-1494) and the Natural Science Foundation of Jiangxi Province (Grant No. 20212BAB213023).

Acknowledgments

Thank you to the reviewers for their valuable feedback on this article, Professor Siripunvaraporn, Xie Maobi, and others for their previous research work, and the editor for their enthusiastic assistance. Thank you to Wenxin Kong for his enthusiastic help.

Conflict of interest

The authors declare that the research was conducted in the absence of any commercial or financial relationships that could be construed as a potential conflict of interest.

Publisher's note

References

Boerner, D. E., Wright, J. A., Thurlow, J. G., and Reed, L. E. (1993). Tensor CSAMT studies at the buchans mine in central newfoundland. *Geophysics* 58 (1), 12–19. doi:10.1190/1.1443342

Cai, H. Z., Xiong, B., and Michael, Z. (2015). Three-dimensional marine controlled-source electromagnetic modelling in anisotropic medium using finite element method. *Chin. J. Geophys.* 58 (08), 2839–2850. doi:10.6038/cjg20150818

Caldwell, G. T., Bibby, M. H., and Brown, C. (2002). Controlled source apparent resistivity tensors and their relationship to the magnetotelluric impedance tensor. *Geophys. J. Int.* 151 (3), 755–770. doi:10.1046/j.1365-246X.2002.01798.x

Cao, H., Wang, K. P., Wang, X. B., Duan, C. S., Lan, X., Luo, W., et al. (2021). Tipper data forward modeling and inversion of three-dimensional tensor CSAMT. *J. Appl. Geophys.* 193, 104432–104441. doi:10.1016/j.jappgeo.2021.104432

Chen, X. Z., Liu, Y. H., Yin, C. C., Qiu, C. K., Zhang, J., Ren, X. Y., et al. (2020). Three-dimensional inversion of controlled-source audio-frequency magnetotelluric data based on unstructured finite-element method. *Appl. Geophys.* 17 (3), 349–360. doi:10.1007/s11770-020-0812-z

Di, Q. Y., Fu, C. M., An, Z. G., Wang, R., Wang, G. J., Wang, M. Y., et al. (2020). An application of CSAMT for detecting weak geological structures near the deeply buried long tunnel of the shijiazhuang-taiyuan passenger railway line in the taihang mountains. *Eng. Geol.* 268 (1), 105517. doi:10.1016/j.enggeo.2020.105517

Garcia, X., Boerner, D., and Pedersen, L. B. (2003). Electric and magnetic galvanic distortion decomposition of tensor CSAMT data. Application to data from the Buchans Mine (Newfoundland, Canada). *Geophys. J. Int.* 154 (3), 957–969. doi:10.1046/j.1365-246X.2003.02019.x

Guo, Z. W., Hu, L. T., Liu, C. M., Cao, C. H., Liu, J. X., and Liu, R. (2019). Application of the CSAMT method to Pb–Zn mineral deposits: a case study in jianshui, China. *Minerals* 9 (12), 726. doi:10.3390/min9120726

He, G. L., Xiao, T. J., Wang, Y., and Wang, G. J. (2019). 3D CSAMT modelling in anisotropic media using edge-based finite-element method. *Explor. Geophys.* 50 (1), 42–56. doi:10.1080/08123985.2019.1565914

Hui, Z. J. (2021) "3D forward modeling and inversion for time-domain marine CSEM based on unstructured finite element method," in *School of Earth exploration science and Technology*. Changchun, China: Jilin University. PhD thesis.

Key, K. (2009). 1D inversion of multicomponent, multifrequency marine CSEM data: Methodology and synthetic studies for resolving thin resistive layers. *Geophysics* 74 (2), F9–F20. doi:10.1190/1.3058434

Key, K. (2016). MARE2DEM: a 2-D inversion code for controlled-source electromagnetic and magnetotelluric data. *Geophys. J. Int.* 207 (1), 571–588. doi:10.1093/gji/ggw290

Kirkby, A., Heinson, G., Holford, S., and Thiel, S. (2015). Mapping fractures using 1D anisotropic modelling of magnetotelluric data: a case study from the Otway Basin, Victoria, Australia. *Geophys. J. Int.* 201 (3), 1961–1976. doi:10.1093/gji/ggv116

Kong, W. X., Yu, N., Li, X., Zhang, X. J., Chen, H., Li, T. Y., et al. (2023). Three-dimensional axially anisotropic inversion of magnetotelluric phase tensor and tipper data. *Chin. J. Geophys.* 66 (9), 3928–3946. doi:10.6038/cjg2023R0040

Li, X. B., and Pedersen, L. B. (1991). Controlled-source tensor magnetotelluric responses of a layered earth with azimuthal anisotropy. *Geophys. J. Int.* 111 (1), 91–103. doi:10.1111/j.1365-246X.1992.tb00557.x

Li, Y., Wu, X. P., Lin, P. R., Han, S. X., Li, D., and Liu, W. D. (2017). Three-dimensional modeling of marine controlled-source electromagnetism using the vector finite element method for arbitrary anisotropic media. *Chin. J. Geophys.* 60 (5), 1955–1978. doi:10.6038/cjg20170528

Li, Y. G., and Key, K. (2007). 2D marine controlled-source electromagnetic modeling: Part 1 — an adaptive finite-element algorithm. *Geophysics* 72 (2), WA51–WA62. doi:10.1190/1.2432262

Liu, X., and Sun, Q.Ji (2024). A study of 3D axis anisotropic response of MT. *Front. Earth Sci.* 12, 1454962. doi:10.3389/feart.2024.1454962

Liu, X., Wang, M., and Chen, B. (2021). 3D tensor CSAMT modeling based on axis anisotropic media. *Chin. J. Prog. Geophys.* 36 (3), 1095–1102. doi:10.6038/pg2021EE0237

Liu, X., and Zheng, F. W. (2024). Axis anisotropic Occam's 3D inversion of tensor CSAMT in data space. *Appl. Geophys.* doi:10.1007/s11770-024-1076-9

Liu, Y. H., Yin, C. C., Cai, J., Huang, W., Ben, F., Zhang, B., et al. (2018). Review on research of electrical anisotropy in electromagnetic prospecting. *Chin. J. Geophys.* 61 (8), 3468–3487. doi:10.6038/cjg2018L0004

Qiu, C. K., Yin, C. C., Liu, Y. H., Chen, H., Liu, L., and Cai, J. (2018). 3D forward modeling of controlled-source audio-frequency magnetotellurics in arbitrarily anisotropic media. *Chin. J. Geophys.* 61 (8), 3488–3498. doi:10.6038/cjg2018L0326

Siripunvaraporna, W., Egbertb, G., and Lenbury, Y. (2002). Numerical accuracy of magnetotelluric modeling: a comparison of finite difference approximations. *Earth Planets Space* 54, 721–725. doi:10.1186/BF03351724

Wang, G., Lei, D., Zhang, Z. Y., Hu, X. Y., Li, Y. B., Wang, D. Y., et al. (2018a). Tensor CSAMT and AMT studies of the Xiarihamu Ni-Cu sulfide deposit in Qinghai, China. *J. Appl. Geophys.* 159, 795–802. doi:10.1016/j.jappgeo.2018.09.031

Wang, K. P., and Tan, H. D. (2017). Research on the forward modeling of controlled-source audio-frequency magnetotellurics in three-dimensional axial anisotropic media. *J. Appl. Geophys.* 146, 27–36. doi:10.1016/j.jappgeo.2017.08.007

Wang, K. P., Tan, H. D., Lin, C. H., Yuan, J. L., Wang, C., and Tang, J. (2018b). Three-dimensional tensor controlled-source audio-frequency magnetotelluric inversion using LBFGS. *Explor. Geophys.* 49 (3), 268–284. doi:10.1071/EG16079

Wang, T., Wang, K. P., and Tan, H. D. (2017). Forward modeling and inversion of tensor CSAMT in 3D anisotropic media. *Appl. Geophys.* 14 (04), 590–605. doi:10.1007/s11770-017-0644-7

Xie, M. B., Tan, H. D., Wang, K. P., Guo, C. A., Zhang, Z. Y., and Li, Z. Q. (2016). Study on the characteristics of 3D CSAMT tensor impedance data. *Chin. J. Prog. Geophys.* 32 (2), 0522–0530. doi:10.6038/pg20170210

Xu, Z. M., Tang, J. T., Li, G., Xin, H. C., Xu, Z. J., Tan, X. P., et al. (2020). Groundwater resources survey of tongchuan city using the audio magnetotelluric method. *Appl. Geophys.* 17 (5-6), 660–671. doi:10.1007/s11770-018-0709-2

Xue, G. Q., Yan, S., Gelius, L. J., Chen, W. Y., Zhou, N. N., and Li, H. (2015). Discovery of a major coal deposit in China with the use of a modified CSAMT method. *J. Environ. and Eng. Geophys.* 20 (1), 47–56. doi:10.2113/JEEG20.1.47

Yin, C. C., Ben, F., Liu, Y. H., Huang, W., and Cai, J. (2014). MCSEM 3D modeling for arbitrarily anisotropic media. *Chin. J. Geophys.* 57 (12), 4110–4122. doi:10.6038/cjg20141222